Fold-change detection and scale invariance of cell–cell signaling in social amoeba

Keita Kamino[a,1], Yohei Kondo[a], Akihiko Nakajima[b], Mai Honda-Kitahara[a], Kunihiko Kaneko[a,b], and Satoshi Sawai[a,b,c,1]

[a]Department of Basic Science, Graduate School of Arts and Sciences, University of Tokyo, Tokyo 153-8902, Japan; [b]Research Center for Complex Systems Biology, University of Tokyo, Tokyo 153-8902, Japan; and [c]Precursory Research for Embryonic Science and Technology, Japan Science and Technology Agency, Saitama 332-0012, Japan

Edited by Peter N. Devreotes, The Johns Hopkins University School of Medicine, Baltimore, MD, and approved April 9, 2017 (received for review February 9, 2017)

Cell–cell signaling is subject to variability in the extracellular volume, cell number, and dilution that potentially increase uncertainty in the absolute concentrations of the extracellular signaling molecules. To direct cell aggregation, the social amoebae *Dictyostelium discoideum* collectively give rise to oscillations and waves of cyclic adenosine 3′,5′-monophosphate (cAMP) under a wide range of cell density. To date, the systems-level mechanism underlying the robustness is unclear. By using quantitative live-cell imaging, here we show that the magnitude of the cAMP relay response of individual cells is determined by fold change in the extracellular cAMP concentrations. The range of cell density and exogenous cAMP concentrations that support oscillations at the population level agrees well with conditions that support a large fold-change–dependent response at the single-cell level. Mathematical analysis suggests that invariance of the oscillations to density transformation is a natural outcome of combining secrete-and-sense systems with a fold-change detection mechanism.

fold-change detection | oscillations | collective behavior | *Dictyostelium* | robustness

Cell–cell signaling lies at the basis of development and maintenance of multicellular forms of life. Extracellular signals are often subject to greater fluctuations in the size of extracellular space and the number of cells (Fig. 1*A*), not to mention nonspecific binding to other molecules, degradation, and dilution. These factors introduce an uncertainty to the detectable number of extracellular ligand molecules, thus posing a threat to the fidelity of cell–cell communication. One of the means by which cells could cope with such uncertainties is to base their behavioral decisions on temporal changes in the extracellular signals. Persistent stimuli are often ignored while their changes in time elicit transient responses—a property collectively called adaptation (1–3). Recent studies have highlighted cellular response whose magnitude appears to be dictated by the fold change in the input stimuli—a property referred to as "fold-change detection" (FCD) (4, 5). In bacterial chemotaxis, cells respond adaptively to a fold change in chemoattractant concentration (6) so that their search patterns depend only on the spatial profiles of the chemoattractant irrespective of its absolute level. Fold-change dependence is also implied in eukaryotic chemotactic response (7, 8) as well as cell fate control and gene regulation in *Xenopus* embryo (9), *Drosophila* imaginal disk (10), and mammalian cells (11). These studies have shed light on the role of FCD for a simple unidirectional signal transduction from an extracellular ligand-receptor interaction (input) to a cellular response (output). However, cell–cell signaling and multicellular systems as a whole often use secretion and sensing of the same molecules (12), whereby the output is fed back to the responding cell itself in addition to the neighboring cells, thus forming a complex bidirectional signal transduction system. The consequence of equipping such systems with an adaptive response and FCD is so far unaddressed.

Oscillations of extracellular cAMP that dictate aggregation of the social amoebae *Dictyostelium discoideum* is a prime example of robust collective behaviors in cell populations. Under starvation, cells synthesize and secrete cAMP, which stimulates other cells in the vicinity to induce further synthesis and secretion of cAMP—a process called "cAMP relay" (13). After prolonged exposure to cAMP, the rise in extracellular cAMP level ceases due to inactivation of adenylyl cyclase (14). As extracellular cAMP level is lowered by degradation, the cells exit from the state of reduced responsivity over the course of several minutes (15, 16), and hence the extracellular cAMP level once again starts to elevate. This tendency for the extracellular cAMP level to rise when it is lowered, and to be lowered when it is raised, essentially renders extracellular cAMP level unstable and oscillatory. The emerging oscillatory waves of extracellular cAMP in the cell population provide a temporal guidance cue for directional cell migration (17, 18). Both cAMP oscillations and cell aggregation are known to occur at a wide range of cell densities spanning at least two to three orders of magnitude (19–22). Cells lacking the cAMP-synthesizing enzyme adenylyl cyclase ACA when ectopically forced to differentiate cannot form aggregates unless they are allowed to randomly collide and form cell clusters at high cell densities (23), indicating that robust cell aggregation depends on intercellular cAMP signaling. Recent live-cell imaging studies have elucidated an input–output relation of the cAMP relay response at the single-cell level resolution (16, 24–26). Although these analyses have implied a role played by the stochastic cAMP relay response at low basal concentrations of extracellular cAMP (~100 pM) in initiating the synchronized pulses, how they could take place robustly in a wide range of cell densities is yet poorly understood.

Results

Density Dependence of the Oscillations. To gain insights on the concentration range of intracellular and extracellular cAMP that

Significance

Recent works have hinted at an ability of cells to respond in the exact same manner to a fold change in the input stimulus. The property is thought to allow cells to function properly regardless of changes in the absolute concentrations of signaling molecules. Despite its general importance, however, evidence has remained scarce. The present work demonstrated that, in the social amoeba *Dictyostelium*, a response to cell–cell communication molecules is fold-change dependent and that this property is tightly linked to the condition that allows them to oscillate collectively, and thus to organize into a multicellular form. Such properties may be of importance for robustness of other developmental systems where oscillatory signaling plays a pivotal role in defining multicellular organization.

Author contributions: K. Kamino, Y.K., K. Kaneko, and S.S. designed research; K. Kamino, Y.K., A.N., and S.S. performed research; M.H.-K. and S.S. contributed new reagents; K. Kamino and A.N. acquired and analyzed live cell image data; K. Kamino and Y.K. performed theoretical and computational analysis; and K. Kamino, Y.K., and S.S. wrote the paper.

The authors declare no conflict of interest.

This article is a PNAS Direct Submission.

Freely available online through the PNAS open access option.

[1]To whom correspondence may be addressed. Email: cssawai@mail.ecc.u-tokyo.ac.jp or k.kamino@amolf.nl.

This article contains supporting information online at www.pnas.org/lookup/suppl/doi:10.1073/pnas.1702181114/-/DCSupplemental.

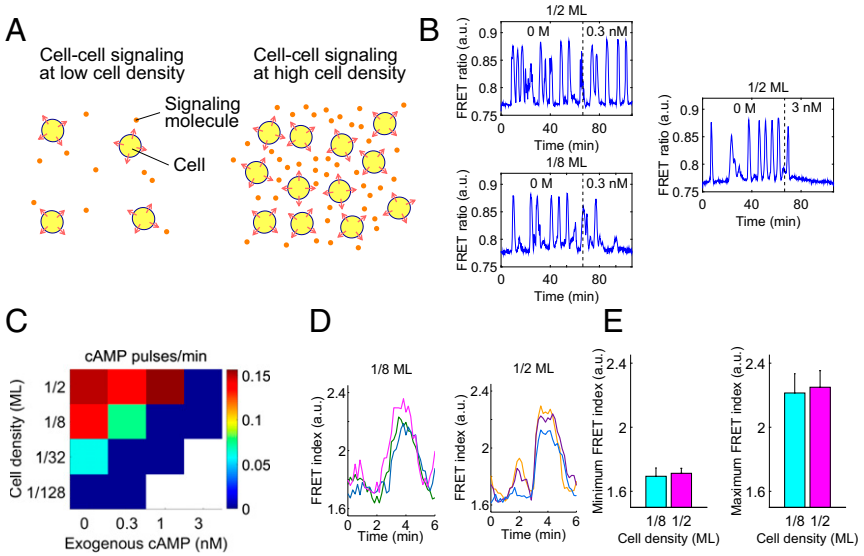

Fig. 1. Dependency of the cAMP oscillations on cell density and the background concentrations of extracellular cAMP. (*A*) A schematic illustrating how variability in cell density introduces uncertainties in the concentration of diffusive signaling molecules. (*B*) Representative time series from Epac1camps (59)-expressing cells (24) before and after application of exogenous cAMP (0.3 nM, 3 nM). Exogenous cAMP (0.3 nM) extinguished oscillations at a low cell density (1/8 ML), whereas almost no clear effect was observed at a high cell density (1/2 ML). (*C*) A phase diagram of the mean pulse frequency as a function of cell density and exogenous cAMP. At high cell densities, the oscillations were relatively insensitive to exogenous cAMP. Squares represent three to six independent measurements of a 2-h duration ($n = 4$, 4, 3, and 3 for 1/2 ML from *Left* to *Right*; $n = 8$, 4, 3, and 3 for 1/8 ML; $n = 4$, 3, and 3 for 1/32 ML; $n = 3$ and 3 for 1/128 ML). (*D*) Representative time series of the FRET index (Epac1camps/AX4 cells) obtained from individual cells oscillating in a population of 1/8 monolayer (ML) (*Left*) and 1/2 ML cell density; perfusion rate, 1.5 mL/min. Colors indicate different cells. (*E*) The average of minimum (*Left*) and maximum (*Right*) FRET index. Error bars represent SD ($n = 21$ for 1/8 ML and $n = 19$ for 1/8 ML).

supports oscillations, we revisited the cAMP dynamics quantitatively by live-cell imaging of cells expressing the cAMP probe Epac1camps (24) combined with a corrected quantification of the fluorescence resonance energy transfer (FRET) efficiency (27) ("FRET index"; Fig. S1 and *SI Materials and Methods*). Collective cAMP oscillations occur spontaneously in cell populations continuously perfused with buffer solution at a moderate flow rate (1.5 mL/min), where extracellular cAMP breakdown by secreted phosphodiesterase (PDE) in vivo is effectively emulated by dilution (24, 28). First, we tested the effect of adding cAMP in the perfusion flow (hereafter refer to as "exogenous cAMP"), which adds on top of endogenously synthesized and secreted cAMP present in the extracellular space. For 0.3 nM exogenous cAMP, the oscillations persisted at a relatively high cell density [1/2 monolayer (ML); 1 ML $\equiv 6.6 \times 10^3$ cells per mm^2] (Fig. 1*B*, *Left Upper*); however, they were extinguished at a lower cell density (1/8 ML) (Fig. 1*B*, *Left Lower*). If we assume cAMP to be the single dominant extracellular factor that dictates the dynamics of cytosolic cAMP, then the results suggest that the concentrations of extracellular cAMP were different under these conditions. Indeed, when the high-cell density cells (1/2 ML) were supplied with higher exogenous cAMP, the oscillations were also extinguished (Fig. 1*B*, *Right*). Systematic analysis of the occurrence of synchronized pulses at various cell densities and exogenous cAMP concentrations showed that the oscillations were more easily suppressed at low cell densities (Fig. 1*C*; vertical axis) and by high exogenous cAMP concentrations (Fig. 1*C*; horizontal axis). On the other hand, the minimum and the maximum of the FRET indices measured at the single-cell level during the cAMP oscillations at low and high cell densities (Fig. 1*D*; 1/2 ML and 1/8 ML) were indistinguishable (Fig. 1*E*), suggesting that the range of cytosolic cAMP concentration during the oscillations does not depend strongly on the cell density. To summarize, the oscillatory range of extracellular cAMP level depends on the cell density and thus is more easily masked by exogenous cAMP at low cell densities, whereas that of the cytosolic cAMP is unchanged.

Rescaled Response Sensitivity. What exact concentration and magnitude change in the extracellular cAMP are required to sustain the collective oscillations? Before and during the early stage of cell aggregation, the basal level of extracellular cAMP slowly builds up and is estimated to reach around 10 nM or less (29, 30), which is near the K_d of the membrane-bound G-protein–coupled receptor CAR1. To see the effect of background concentrations of extracellular cAMP in this range, we measured single-cell level cAMP relay responses in well-isolated cells ($<10^{-3}$ ML) (24) that were first primed with a fixed concentration of cAMP (0.1, 1, 3, and 10 nM) for about 40 min to let the initial response attenuate before elevating the cAMP level in a step-like manner (*Materials and Methods*). Note that, in contrast to the population-level oscillation experiments described in the previous section, here, care was taken so that cAMP secreted by the cells becomes negligible (24); extracellular buffer was rapidly diluted by fast perfusion (4–8 mL/s; *Materials and Methods*), cells were plated at low cell densities (see *Materials and Methods*), and a cell was chosen for observation after confirming that there is no other cell within the surrounding area of ~0.3-mm radius. Fig. 2*A* shows reference time courses of the cAMP relay response to a step increase in the extracellular cAMP concentration from 0 to 3 nM, a nonprimed stimulus condition that elicits a maximum amplitude response as measured by the FRET signal (24). The level of cytosolic cAMP reached the maximum at 2–3 min after the stimulus application followed by secondary peaks that slowly attenuated in close agreement with a previous study (24). Under primed conditions, the response to 3 nM on top of 1 nM extracellular cAMP was markedly reduced in both initial and secondary peak amplitude (Fig. 2*B*, *Left*), whereas elevation from 1 to 10 nM induced a large magnitude response (Fig. 2*B*, *Right*) comparable to that observed under nonpriming conditions.

Next, we quantified the initial peak amplitude 2–3 min after the stimulus increase. This serves as the primary measure of the strength of the relay response underlying the collective oscillations, because the secondary peaks were not observed when the level of extracellular cAMP was elevated only for a few minutes

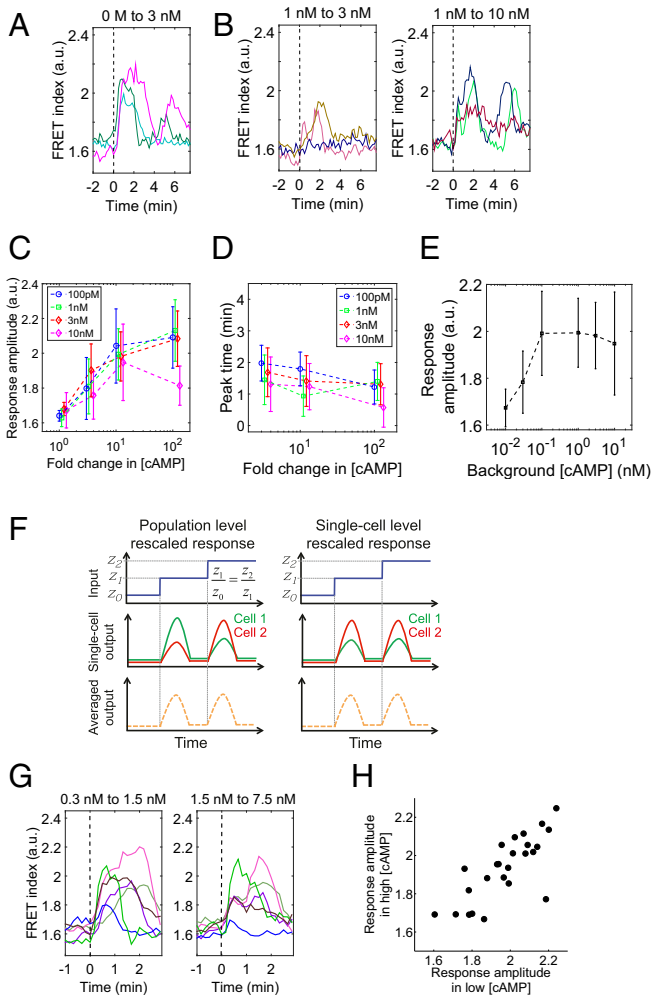

Fig. 2. The cAMP relay response at the single-cell level obeys fold-change detection. (*A* and *B*) The concentration of perfused cAMP was changed from 0 to 3 nM (*A*), 1 to 3 nM (*B*; *Left*), and 1 to 10 nM (*B*, *Right*). The dotted lines indicate the time of stimulus switch. Colors indicate different cells. (*C* and *D*) The peak amplitude (*C*) and the response time (*D*) of the response; priming concentrations, 0.1 nM (blue), 1 nM (green), 3 nM (red), and 10 nM (magenta) cAMP. The vertical axis: the maximum FRET index during the 4 min after the input change (*C*) and the time it took for the FRET index to reach the initial peak (*D*). Dots and error bars indicate the mean and SD (n = 11, 16, 16, and 15 for 1-, 3-, 10-, and 100-fold change from 100 pM, respectively. In the same way, n = 13, 23, 15, and 16 for 1 nM; n = 11, 13, 11, and 14 for 3 nM; n = 16, 7, 10, and 9 for 10 nM). (*E*) The amplitude of the response to 10-fold increase in the extracellular cAMP concentration. Error bars indicate SD (n = 10, 14, 16, 15, 11, and 10 for 10^{-2}, 3×10^{-2}, 0.1, 1, 3, and 10 nM, respectively). (*F*) Two possible scenarios for the curves in *C*. (*Left*) The response sensitivity is heterogeneous and not rescaled at the single-cell level. (*Right*) The response sensitivity rescales at the single-cell level. (*G*) Representative responses to sequential fivefold step inputs from 0.3 to 1.5 nM (*Left*), and then from 1.5 to 7.5 nM (*Right*). Colors are mapped to identify individual cells consistently in two panels. Cells were kept at 1.5 nM cAMP for 15 min before the second increment. (*H*) A scatter plot of the response amplitude to two incremental step inputs; correlation coefficient, 0.68 (n = 25).

(24) (Fig. S2*A*) as is the case during the collective oscillations. Fig. 2*C* plots the index as a function of fold increase in extracellular cAMP concentration for four priming concentrations tested. For priming concentrations below 10 nM (0.1, 1, and 3 nM), the plots collapsed on a single curve, indicating that, within this concentration range, the single major determinant of the peak amplitude of the cAMP relay response is the fold change in the extracellular cAMP concentration. The peak FRET index observed during the relay response was half-maximal at about a 3-fold increase in the extracellular cAMP concentration and levels off at about a 10-fold increase. The time at which the initial peak reached the maximum value showed almost no dependency on the background level of extracellular cAMP (Fig. 2*D*). Moreover, the amplitude of the response to a fold change of 10 was more or less constant between 0.1 and 10 nM background concentrations (Fig. 2*E*), suggesting that the rescaling property holds for two orders of magnitude. The same rescaling property was also observed when the step-stimulus was repeated (Fig. S2*A*).

One should note that an apparent fold-change dependence in the population-averaged response (Fig. 2*C*) should not be readily equated with a fold-change detection at the single-cell level. For example, cell–cell variability in the response sensitivity alone in the absence of FCD could deceptively bring about a similar response curve after averaging (Fig. 2*F*, *Left*). In principle, whether or not rescaling holds at the level of individual cell (Fig. 2*F*, *Right*) should be tested by measuring the response to fold-change stimulus numerous times in single cells. However, this is not feasible due to phototoxicity and also because cells differentiate in the timescale of hours. Instead, we measured the response to two incremental steps with a fold change of 5 (0.3, 1.5, and 7.5 nM cAMP). Fig. 2*G* shows representative time series of single-cell level responses. Those cells that show weak response in the initial increment also tend to show weak response in the second increment. Likewise, cells with large response were consistent in two incremental stimuli. Despite a large cell–cell variability in the amplitude, the variability was spread along a linear slope in the scatter plot (Fig. 2*H*). In other words, the amplitudes of the response to the consecutive inputs were highly correlated in each individual cells. The results indicate that the fold-change dependence is a single-cell level property.

During cell aggregation of *Dictyostelium discoideum*, synchronous emission of cAMP gives rise to periodic traveling waves of extracellular cAMP, and thus the level of extracellular cAMP is oscillating (29). In this respect, the spatially uniform and temporally abrupt stimulus used in the above section deviates from the naturally occurring one. In general, a response to a step stimulus may not necessarily have the same propensity as that for a slowly varying stimulus. Moreover, directional migration is induced by a traveling-wave stimulus (17, 18) and thus may affect the cAMP relay owing to a large overlap in the signal transduction network (16, 31, 32). To test relevance of the fold-change response property for natural cAMP wave, we used a microfluidics lighthouse (33)—a gradient-generating platform capable of delivering traveling-wave stimulus of various amplitude, frequencies, and speed. Using this device, we applied 6-min period cAMP stimuli to cells in the region of interest (Fig. 3*A*; dotted square) in the form of spatially symmetric bell-shaped gradient that measures ∼500 μm from the trough to the peak and traversed at a speed of ∼2–3 × 10^2 μm/min (Fig. 3 *A* and *B*), which closely follows the estimated parameters of natural cAMP waves (34). The flow is slow and does not bias directionality of cell migration (33), and there is no apparent shear-induced effect on the level of cytosolic cAMP (Fig. 3*C*). Fig. 3 *D*–*F* shows representative responses of well-isolated cells to repetitive wave stimulus with fold increase/decrease of 30 for background concentration of 0.1, 1.0, and 3.0 nM extracellular cAMP. In all three conditions, albeit cell–cell variability, the concentration of cytosolic cAMP in individual cells oscillated in phase with that of extracellular cAMP whose peak time showed delay of ∼10–40 s. The peak FRET index was on average almost constant under these conditions (Fig. 3*G*), confirming that the magnitude of single-cell level response to traveling-wave stimulus is fold-change dependent.

The cAMP relay response is mediated by complex signaling cascades downstream of G-protein–coupled receptors that are yet to be

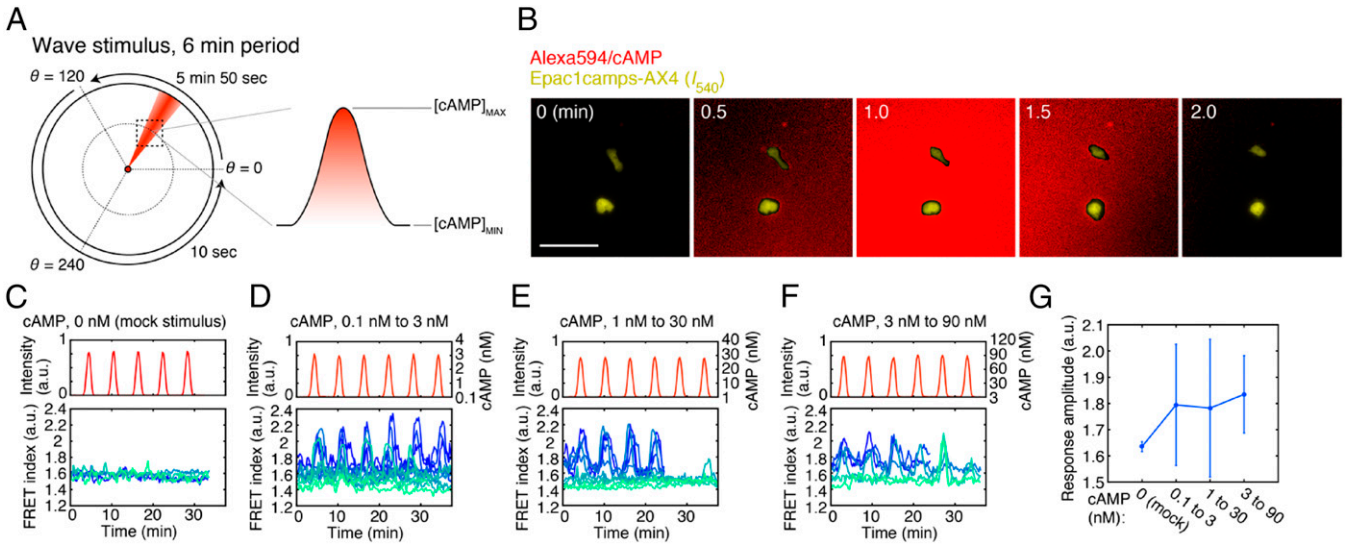

Fig. 3. The cAMP relay response to traveling-wave stimuli. (*A*) Application of a traveling-wave stimulus using the lighthouse device (33). A schematic of generating periodically rotating waves at 6-min period (*Left*). Due to diffusion, a bell-shaped gradient forms perpendicular to the flow of buffer solution containing high concentration of cAMP (red). The orientation of the stimulus flow was varied at the rate of 0.34°/s anticlockwise from $\theta = 0°$ to 120°, thereby allowing a bell-shaped gradient to traverse the observation area (dotted square). For the remaining region from $\theta = 120°$ to 360°, the rotation was fast-forwarded by switching the direction discretely in two steps from 120° to 240°, and then 240° to 360° (33). Alexa Fluor 594 was included in the stimulus solution to estimate the spread of cAMP. For each run of experimental observation, the rotation was cycled four to six times. (*B*) Merged confocal images of the stimulus profile (red; Alexa) and Epac1camps/AX4cells [yellow; YFP (I_{540nm}) channel] during a wave passage. (Scale bar, 50 μm.) (*C–F*) cAMP response to the wave stimulus. cAMP concentrations: mock (*C*; $n = 5$ cells), 0.1–3 nM (*D*; $n = 12$ cells), 1–30 nM (*E*; $n = 10$ cells), and 3–90 nM (*F*; $n = 6$ cells). Temporal profiles of the wave stimulus (*Upper*) and individual cell responses (*Lower*; graded blue green colors indicate different cells). Buffer solution containing Alexa Fluor 594 without cAMP was used for the mock control (*C*). cAMP concentrations were estimated from the fluorescence intensity of the Alexa dye (*D–F*). (*G*) The average peak FRET index. Error bars indicate SDs.

fully revealed (31, 35). Binding of extracellular cAMP to the receptor activates small GTPase Ras, which then activates phosphoinositide 3-kinase (PI3K) to elevate phosphatidylinositol-(3,4,5)-triphosphate (PIP_3) at the plasma membrane (36). PIP_3 serves as a docking site for a pleckstrin homology (PH) domain-containing protein cytosolic regulator of adenylyl cyclase (CRAC) that is essential for the activation of adenylyl cyclase ACA (37, 38). These activation processes are counteracted by deactivation of Ras by RasGAP (39) and conversion from PIP_3 to PIP_2 by phosphatase PTEN (40). Less is known about adaptation of ACA besides the fact that it depends on receptor phosphorylation (41) and PI3K (16, 38). Semirescaling of the response sensitivity has been reported at the level of Ras activation (42), which appears "FCD-like" after population averaging (7, 8).

To gain further insights into how the rescaling property is embedded at an event closely upstream of ACA, we measured membrane translocation of PH domain of CRAC (37) fused to RFP (PH_{CRAC}-RFP) (43) (*Materials and Methods*; Fig. S3). In the perfused cell populations, the FRET index and PH_{CRAC}-RFP translocation oscillated in phase at the single-cell level (Fig. 4*A* and Movie S1) with delay of no more than 1 min as evident by the cross-correlation analysis (Fig. 4*B*). In isolated cells exposed to rapid step stimuli (50% exchange of extracellular solution in less than 10 s), the correlation between the membrane translocation of PH_{CRAC}-RFP and the cAMP relay response at the single-cell level was less apparent. The transient translocation of PH_{CRAC}-RFP from the cytosol to the plasma membrane occurred within 10–20 s after the stimulus elevation, which is in contrast to the cAMP relay response that took close to 2 min to reach its peak. Fig. 4*C* shows the time course of PH_{CRAC}-RFP translocation in isolated cells at different priming concentrations (*Materials and Methods*). Similar to the cAMP relay response, for 0.1 and 1 nM priming concentrations of cAMP, the degree of membrane translocation of PH_{CRAC}-RFP exhibited a fold-change dependency (Fig. 4*D*). The time it took for the response to reach its peak also appeared almost identical (Fig. 4*E*) with a slight decline at a higher fold stimuli as has been noted for Ras activation (7). Rescaling of the response sensitivity was observed in a somewhat narrower range of the background cAMP concentrations (~0.1–1 nM) (Fig. 4*F*) compared with that of the cAMP relay response (~0.1–10 nM) (Fig. 2*E*). On average, there was decrease in the degree of PH_{CRAC}-RFP translocation at priming concentrations higher than 1 nM. These results suggest that information regarding fold change in the extracellular cAMP concentration is encoded and transduced, at least partially, by the degree of membrane translocation of CRAC.

Scale Invariance of FCD-Based Signaling. How are the input–output properties revealed at the single-cell level related to the oscillatory behavior at the population level? Let us formulate a secrete-and-sense system where the output "*y*" is determined by the input signal "*z*"; conversely, the input *z* is determined by the response *y*. To this end, we shall first describe a ligand-induced response by a two-variable system $\dot{x} = f(x,y;z)$, $\dot{y} = g(x,y;z)$, where intracellular and extracellular cAMP are represented by *y* and *z*, respectively (Fig. 5*A*). Here, *x* is an internal variable required for adaptation. Mathematically, the system obeys FCD when the functions *f* and *g* satisfy a condition:

$$f(\phi(p,x),y;pz) = \frac{\partial\phi(p,x)}{\partial x} f(x,y;z)$$
$$g(\phi(p,x),y;pz) = g(x,y;z), \qquad [1]$$

with an appropriate transformation function ϕ and an arbitrary scaling factor p (>0) (5) (*SI Equations*). Under this constraint, the variable *y* responds in an identical manner to two incremental *p*-fold increase in the input *z* (Fig. 5*B*). By introducing a third equation that

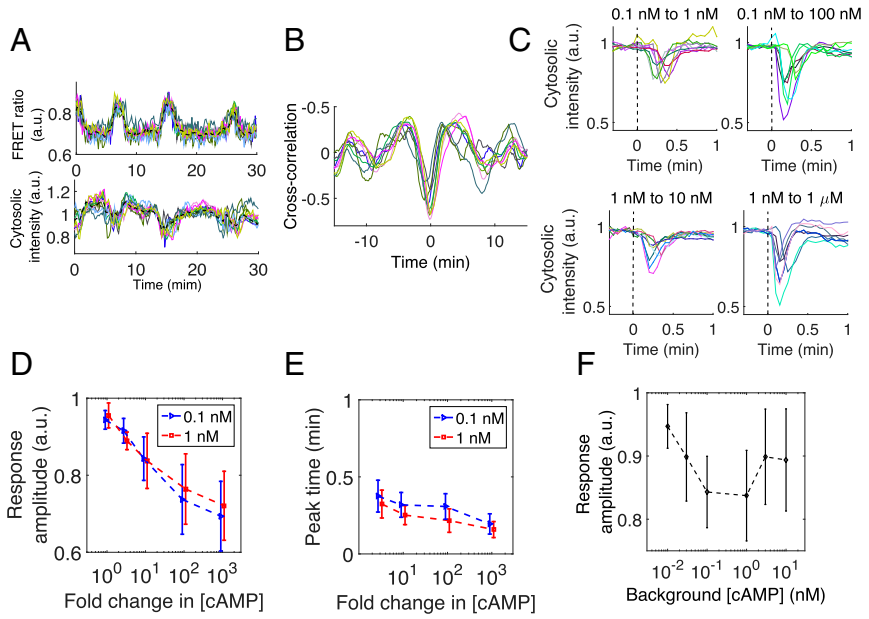

Fig. 4. Rescaling of the response sensitivity in an ACA activating pathway. (*A*) Simultaneous measurements of cytosolic cAMP (*Upper*) and PH_{CRAC}-RFP (*Lower*) (Epac1camps/PH_{CRAC}-RFP/AX4 cells; 1/2 ML density). Representative data taken from cells chosen randomly from a field of view ($n = 10$). Colored lines indicate single-cell data, and the black line represents the average. (*B*) Cross-correlations for single-cell data. (*C*) Representative time courses of PH_{CRAC}-RFP membrane translocation after a 10-fold (*Left*) or 10^3-fold (*Right*) increase in the extracellular cAMP concentration. Colors indicate different cells. (*D* and *E*) The amplitude (*D*) and the response time (*E*) of PH_{CRAC}-RFP membrane translocation after an increase in the extracellular cAMP concentrations from 0.1 and 1 nM. Error bars represent SD ($n = 21$, 18, 30, 31, and 28 for 1-, 3-, 10-, 100-, and 1,000-fold change from 0.1 nM, respectively. Likewise, $n = 18$, 19, 28, 46, and 30 for 1 nM). The minimum cytosolic fluorescence intensity for the first 1 min after the input change (*D*; vertical axis). The time it took for the cytosolic intensity to reach the minimum value (*E*). (*F*) The response amplitude to 10-fold increase in extracellular cAMP. Mean and SD are shown ($n = 18$, 22, 30, 28, and 17 for 10^{-2}, 3×10^{-2}, 0.1, 1, 3, and 10 nM, respectively).

describes the dynamics of extracellular cAMP z in a perfusion chamber (13, 24), we arrive at a closed-loop system (Fig. 5*C*):

$$\begin{aligned}\dot{x} &= f(x,y,z)\\ \dot{y} &= g(x,y,z)\\ \dot{z} &= \rho k_t y - \gamma z,\end{aligned} \qquad [2]$$

where ρ, k_t, and γ represent the cell density, the secretion rate, and the dilution rate, respectively. The extracellular cAMP z affects the dynamics of the cells—that is, the subsystem x and y; hence the system describes "sensing and secretion" of the same molecules (12, 44).

From the above mathematical formulation, it is readily shown that Eq. **2** are invariant under a transformation; that is, $(x,y,z,\rho) \to (\phi(p,x),y,pz,p\rho)$ (see *Supporting Information* for proof). The scale invariance ensures that, although extracellular cAMP (z) scales with the cell density, the intracellular cAMP y, regardless of whether it is a fixed constant or dynamically changing variable, remains unaffected by density transformation $\rho \to p\rho$. Because the invariance derives simply by requiring the FCD condition (Eq. **1**) for the response dynamics (Eq. **2**; equations for x and y), and combining them with the secretion/dilution dynamics (Eq. **2**; the equation for z), it can be said that the robustness of the cAMP oscillations to variation in cell density is a natural outcome of the observed response-rescaling property of the constituent cells. Note that, for the sake of clarity, the above derivation assumed that the response functions $f(x, y; z)$ and $g(x, y; z)$ are the same in all cells. The conclusion holds when there is cell–cell variability (*SI Equations*; Eqs. **S6** and **S7**).

Scale Invariance of the cAMP Oscillations. To obtain networks that exhibit adaptive response that obeys FCD, which could then be combined with the equation for z (Eq. **2** and Fig. 5*C*), a computational search for minimal networks with two nodes and three links (3, 45, 46) was performed (Fig. S4 *A*–*C*). Four networks were identified: two "incoherent feedforward loop" type (Fig. S4*D*) and two negative-feedback loops type (Fig. S4*E*), which are consistent with recent analytical search of a topology space (46). The basic network models could be slightly modified to take into account the nonlinear input–output relation of the cAMP relay response (Fig. 2*C*) while preserving the network topology and the FCD property (*SI Equations*). Although details of the response can be compared to further constrain the network topology (26, 47–49), the present aim is rather to understand the general outcome of incorporating FCD in a secrete-and-sense system. Qualitative features detailed below were conserved in all four selected network types (Fig. S5). For brevity of presentation, a feedforward-type network,

$$\begin{aligned}\tau\dot{x} &= z - x\\ \dot{y} &= \frac{z^n}{z^n + (Kx)^n} - y\\ \dot{z} &= \rho k_t y - \gamma z,\end{aligned} \qquad [3]$$

is described below (*SI Equations*, model [**A″**]). Parameters τ, n, and K are positive constants. The feedforward network depicts receptor-mediated signals that induce both fast activation and slow terminating reactions (1) and is compatible with adaptation and deadaptation of adenylyl cyclase that depend strictly on elevation and lowering of the extracellular cAMP level, respectively. Earlier mathematical models of cAMP relay (50, 51) as well as chemotaxis models that describe conversion between GTP-bound and GDP-bound form of Ras (42) also have this network topology.

With an appropriate choice of parameter values, the system (Eq. **3**) exhibited oscillations (Fig. 5*D*). The oscillatory solution in the present model (Eq. **3**), especially the level of intracellular

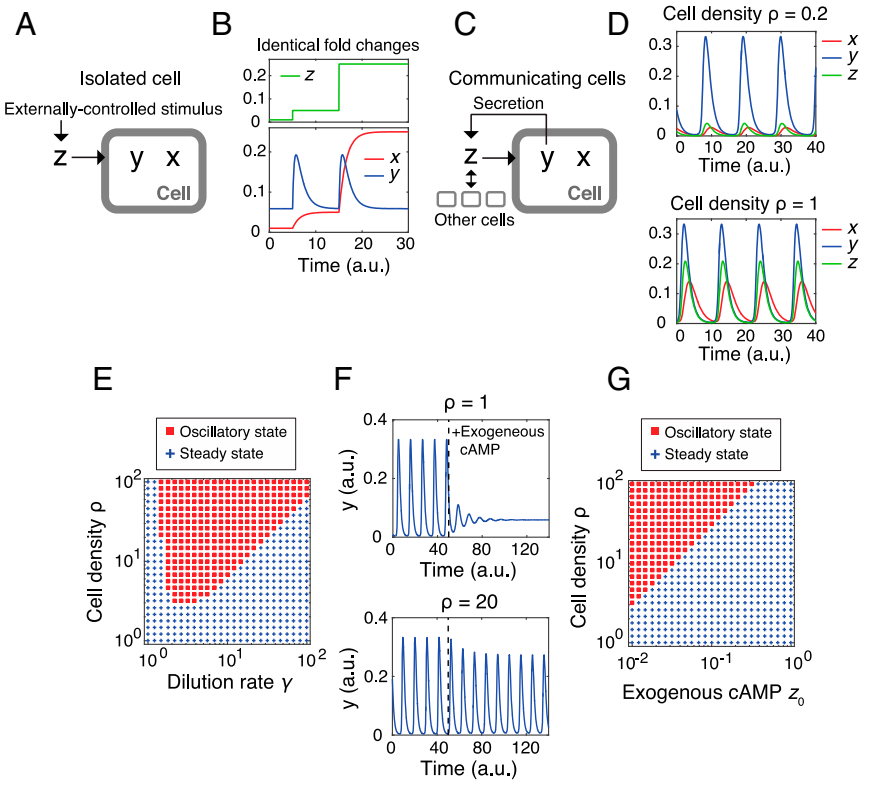

Fig. 5. Density robustness is a basic property of a secrete-and-sense system consisting of FCD elements. (*A* and *B*) A reaction scheme (*A*, "Isolated Cell") and the characteristic behaviors (*B*) of an FCD system. The time evolution of *y* and *x* are described by functions *f* and *g* that together constitutes a FCD system (*A*). Simulated time course of *x* and *y* (*B*, *Lower*) to incremental increase in z (*B*, *Upper*). (*C* and *D*) A Schematic diagram of a closed-loop secrete-and-sense system (*C*, "Communicating cells") and results from model simulations (Eq. **3**) for low (*Upper*) and high (*Lower*) cell densities. Here, *x* and *y* follow the same reaction scheme as in *A* except that *y* is secreted, and thus transformed to *z* to further stimulate the cells. (*E*) A phase diagram of the system (Eq. **3**) with a lower detection limit. Oscillatory (red squares) and static [blue plus sign (+)] states. (*F*) Results from numerical simulations of a modified model (Eq. **3** with $dz/dt = \rho k_t y - \gamma(z - z_0)$). (*G*) A phase diagram of the system (the model in *D*) as a function of cell density ρ and the exogenous cAMP level z_0. Red squares and blue plus signs (+) indicate oscillatory and static states, respectively. The parameters were $\tau = 1.5$, $n = 2$, $K = 4$, $k_t = 2$, and $\gamma = 3$, unless otherwise indicated.

cAMP *y*, is insensitive to the value of ρ (Fig. 5*B*) owing to the scale invariance resulting from the FCD property. This feature is in marked contrast with earlier models (50, 51) where oscillations were observed only in a narrow range of cell density (less than one order of magnitude) irrespective of the dilution rate γ [for model (50), see Fig. S6]. With further inclusion of lower detection limit by replacing z by $z + \delta$ on the right-hand side of the equations for x and y (Eq. **3**), where δ is a positive constant parameter (*SI Equations*), we see that the lower limit of cell density that supports collective oscillations becomes a monotonically increasing function of the dilution rate (Fig. 5*E*)—in agreement with earlier experimental data (figure 2*B* in ref. 24).

The most important suggestion of the present model is that the range of extracellular cAMP level that confers fully periodic collective oscillations should be dictated by the operation range of FCD. Such a view is supported from the estimates of the extracellular cAMP concentration at various cell densities. Under typical experimental parameters, owing to the high dilution rate ($\gamma \sim 6\ \mathrm{min}^{-1}$ in the present study) compared with the timescale of intracellular cAMP dynamics ($\sim 1/7\ \mathrm{min}^{-1}$), the concentration of extracellular cAMP (z) can be estimated by applying quasi–steady-state approximation (*SI Equations*). At cell densities of 1/2 and 1/8 ML, where population of cells exhibited cAMP oscillations at a constant high frequency (Fig. 1*C*) (24), the estimated basal concentrations of extracellular cAMP are 0.72 nM for 1/2 ML and 0.18 nM for 1/8 ML, which are well within the FCD range (Fig. 2*E*; ≥0.1 nM). At 1/32 and 1/128 ML where populations showed sporadic or no oscillation, the estimated extracellular cAMP are 0.05 nM for 1/32 ML and 0.01 nM for 1/128 ML, which lie at the border or outside the FCD range (Fig. 2*E*; <0.1 nM). Thus, the conditions that support full-amplitude ~7-min period oscillations agree well with the FCD range.

The critical relation between FCD and the oscillatory conditions is also vindicated by the suppression of oscillations in the presence of exogenous cAMP and/or at low cell densities as demonstrated experimentally (Fig. 1 *B* and *C*) as well as in the numerical simulations (Fig. 5*F*). Here, the model equations were extended to include the influx of exogenous cAMP (z_0) by rewriting the equation for z as $dz/dt = \rho k_t y - \gamma(z - z_0)$, which now violates the condition for scale invariance. The phase diagram in the parameter space (z_0, ρ) obtained numerically shows a linear slope that demarcates the oscillatory and nonoscillatory domains (Fig. 5*G*), which closely resembles the phase diagram obtained experimentally (Fig. 1*C*). The feature of the phase diagram can be understood by the fold-change responsiveness of the constituent cells as follows. Under no exogenous cAMP, the estimated fold change in the extracellular cAMP level during the oscillations is $z_{\mathrm{peak}}(\rho)/z_{\mathrm{basal}}(\rho)$, where z_{peak} and z_{basal} are the peak and basal concentrations of extracellular cAMP, respectively, both of which increase as a function of cell density (*SI Equations*). Conversely, in the presence of exogenous cAMP, the estimate would be $A_z(\rho, z_0) = (z_{\mathrm{peak}}(\rho) + z_0)/(z_{\mathrm{basal}}(\rho) + z_0)$. Because A_z is a decreasing function of z_0 and increasing function of ρ, at higher concentrations of exogenous cAMP and/or at lower cell densities, the response becomes small and less likely to sustain oscillations. Our single-cell data (Fig. 2*C*) indicate that the change in the level of extracellular cAMP should be greater than ~10-fold;

otherwise, the response amplitude was markedly diminished, and there were no population-level oscillations. Consistent with such a view, the values of A_z for conditions that supported the oscillations were always higher than those in the nonoscillatory conditions and the border between the two domains was at $A_z \sim 10$ (Table S1). These results suggest that the secrete-and-sense system that consists of FCD elements captures the essence of the density dependence of the oscillations.

Discussion

The present study demonstrated that the cAMP relay response is adaptive and fold-change dependent at low extracellular cAMP concentrations (≤10 nM). Based on the observed input–output relation, we proposed a model that consists of elements that obey FCD that well describes the cell density and extracellular cAMP conditions that support the population-level oscillations. Recently, an alternative model based on the Fitzhugh–Nagumo equations was proposed (26). There, it is thought that population-level oscillations emerge as a result of a stochastic threshold-like response to fluctuating levels of extracellular cAMP. Such a view contrasts markedly with the model proposed here where a positive-feedback loop between intracellular and extracellular cAMP and adaptation of the response give rise to oscillations—a deterministic scheme that shares its core idea with other earlier models (50). The appearance of frequency selectivity and a refractory period (26) do not suffice as a criteria for model selection as these behaviors were also reproduced in the current adaptation-based model (Fig. S2 *B* and *C* and *SI Discussion*). Experimentally, the obtained dose–response (Fig. 2*C*) had no clear threshold but rather increased gradually—a feature not in support of an excitable noise-driven mechanism. Moreover, according to the Fitzhugh–Nagumo-type mechanism, inclusion of exogenous cAMP should give rise to more pulses of cAMP by increasing the chance to cross the response threshold. Our observations were quite the opposite. The oscillations were suppressed by exogenous cAMP (Fig. 1 *B* and *C*). Despite these caveats, we should note that the Fitzhugh–Nagumo-based model captures the sustained (i.e., nonadaptive) oscillatory response behavior (26) that occurs under prolonged stimulus in the non-FCD range (>10 nM cAMP) (24). These oscillations are driven intracellularly without the need for clearing of extracellular cAMP—a feature in favor of the Fitzhugh–Nagumo-type scheme. For the population-level oscillations, in contrast, a strict dependency on extracellular cAMP clearing has been demonstrated by a null-mutant of extracellular phosphodiesterase that cannot oscillate unless it is cleared of extracellular cAMP by perfusion (28). It may be that different cAMP receptor forms (52) or receptor types (53) with different binding constants transduce FCD and non-FCD signals.

The present analysis and the proposed theoretical framework suggest that, when an adaptive response governed by FCD is incorporated into a "secrete-and-sense" circuitry (12, 44), the resulting cell–cell communication is robust to cell density change due to the scale-invariant property of the system equations. In the present analysis, the extracellular signaling molecule z is described by a relatively simple equation owing to the first-order secretion kinetics (13) and the constant dilution rate realized by perfusion. In addition, density robustness can also be realized in more complex situations, for example, nonlinear secretion kinetics, a density-dependent degradation rate, and spatial inhomogeneity (*SI Equations*, Fig. S7, and *SI Discussion*). Although the FCD mechanism could explain the ability of *Dictyostelium* cells to execute aggregating behavior at a wide range of cell density (21, 22), the present findings do not rule out other mechanisms that may be at work in conjunction. cAMP-dependent regulation of a gene encoding extracellular PDE can provide robustness (28), in this case by keeping the level of extracellular cAMP within a desirable range. Cell–cell heterogeneity in the response sensitivity could also render oscillations robust to cell density change (Fig. 2*F*, *Left*). We should note, however, that FCD at the single cell–level (Fig. 2*H*) alleviates the requirement for averaging over many cells, which could be critical in nature where averaging is limited by diffusion. Given the ubiquity of adaptation and secrete-and-sense circuits (12), FCD-based robustness may have a wide connotation in other multicellular phenomena. A case in point is the collective oscillations of NADH in yeast cell suspension whose amplitude and frequency are conserved for three orders of magnitude in cell density (54). In higher organisms, morphogen fields are dynamic and their temporal changes appear to be read out to regulate cell fates (10, 55). Traveling waves are also prevalent in embryonic development (56, 57). It would be interesting to explore whether the same mathematical principle applies in these and other systems.

Materials and Methods

Strains and Cell Culture. *Dictyostelium discoideum* AX4 cells expressing Epac1camps (Epac1camps/AX4) (24), PH domain of CRAC fused to monomeric red fluorescent protein (mRFP) (PH_{CRAC}-RFP/AX4) (43), and both PH_{CRAC}-RFP and Epac1camps (Epac1camps PH_{CRAC}-RFP/AX4) were used. For coexpression, Epac1camps/AX4 cells were transformed with PH_{CRAC}-RFP expression vector by electroporation. A clonal isolate showing normal development with relatively bright fluorescent for both probes was used for the analysis. Cells were grown at 22 °C in PS medium (58) with 10 μg/mL G418 and/or 60 μg/mL hygromycin B, where appropriate. Typically, 30-mL cell culture was shaken in an Erlenmeyer flask (250 mL; Bellco) at 155 rpm (Taitec; BR43-FL). Cells were propagated below ∼2×10^6 cells per mL. For live-cell imaging, cells were removed from growth medium by centrifugation for 3 min at 700 × *g* followed by resuspension in fresh developmental buffer (DB) (10 mM K/Na_2 phosphate buffer, 1 mM $CaCl_2$, 2 mM $MgCl_2$; pH 6.5). The washing step was repeated twice. The cells were resuspended in ∼1-mL DB at ∼2×10^7 cells per mL and allowed to differentiate for 4–5 h in a centrifuge tube shaken at 155 rpm (Taitec; BR43-FL).

Perfusion and Live-Cell Microscopy. Starved cells were plated on a glass-bottom dish at a cell density below 1×10^3 cells per cm^2, and a perfusion chamber was constructed using an insert (RC-37F; Warner Instruments) as previously described (24), with the exception of results shown in Fig. 3, which used the lighthouse device (33) (*SI Materials and Methods*). After cells have attached to the bottom of the chamber, DB was perfused to remove effects from past stimuli at the rate of 4–8 mL/min, unless otherwise noted. For the cAMP relay study, the flow rate was kept at 8 mL/min for longer than 1 min before and after stepwise changes in the cAMP concentrations. At the given flow rate, one-half of the solution in the chamber was exchanged within 10 s as tested by monitoring fluorescein solution under a microscope. When there is no need to change the stimulus level, the flow rate was reduced to 4 mL/min. For observations of population-level cAMP oscillations, the flow rate was 1.5 mL/min.

Epifluorescent live-cell imaging of Epac1camps/AX4 cells was performed essentially as described in the previous work (24) using the same inverted microscopy system. In the present study, images were taken at 10- to 15-s intervals for total duration of ∼0.5–2 h. In addition, an image from the YFP channel was acquired to correct for cross-excitation immediately before time-lapse acquisition (*SI Materials and Methods*). To this end, cells were exposed for 30 ms with 495-nm light using an excitation filter (BP490-500HQ; Olympus), which was further attenuated by 6% using neutral density filters. The emitted light was separated from the excitation by a dichroic mirror (DM505; Olympus).

Confocal imaging of PH_{CRAC}-RFP/AX4 and PH_{CRAC}-RFP Epac1/AX4 was performed using an inverted microscope (IX-81; Olympus) equipped with an automated stage (BIOS-215T; Sigma Koki), a confocal scanning unit (CSU-X1; Yokogawa), and optical shutters (LS6ZM2; Uniblitz Electronics). An oil-immersion objective lens (60× PlanApo N, N.A. 1.42, or 20× UPlanSApo N, N.A. 0.85; Olympus) was used. The stage and the shutters were controlled by a stage controller (FC-101G; Sigma Koki) and a shutter driver (VMM-D3; Uniblitz Electronic), respectively. The device control and data acquisition were conducted using the Metamorph software (Molecular Devices). A 445-nm laser (40 mW; Vortran Laser Technology) and a 561-nm laser (25 mW; Melles Griot) were used as light sources. For imaging PH_{CRAC}-RFP, cells were exposed to 561-nm laser for 30 ms. The laser was attenuated by 50% with a neutral density filter. The fluorescent light was passed through an emission filter (BA575IF; Olympus). For Epac1camps-expressing cells, 445-nm laser attenuated by 50% using neutral density filters was applied for 50 ms. A set

of multiband dichroic mirror and filters (CFP/YFP/HcRed-3X3M-A; Semrock) was used except for the CFP excitation filter (BP425-445HQ; Olympus). Sixteen-bit 512 × 512 pixel images were captured at 3- to 10-s interval using an EMCCD camera (Evolve 512; Photometrics). All image acquisition was performed at 22 °C. Data were stored in tagged image file format (TIFF) files.

ACKNOWLEDGMENTS. We thank all members of the S.S. Laboratory and the K. Kaneko Laboratory and T. S. Shimizu for stimulating discussions, P. R. ten Wolde for suggestions on an earlier version of the manuscript, and V. O. Nikolaev and M. J. Lohse for providing an Epac1camps plasmid. This work was supported by Japan Society for the Promotion of Science KAKENHI Grants JP25710022, JP15KT0076, JP16H01442, JP25103008 (to S.S.), and JP16K18537 (to A.N.); Fellows Grant 23-10097 (to K. Kamino); Japan Science and Technology Agency Precursory Research for Embryonic Science and Technology Grant JPMJPR11AD (to S.S.); and the Agency for Medical Research and Development, Platform for Dynamic Approaches to Living System.

1. Devreotes PN, Steck TL (1979) Cyclic 3′,5′ AMP relay in *Dictyostelium discoideum*. II. Requirements for the initiation and termination of the response. *J Cell Biol* 80: 300–309.
2. Koshland DE, Jr, Goldbeter A, Stock JB (1982) Amplification and adaptation in regulatory and sensory systems. *Science* 217:220–225.
3. Ma W, Trusina A, El-Samad H, Lim WA, Tang C (2009) Defining network topologies that can achieve biochemical adaptation. *Cell* 138:760–773.
4. Goentoro L, Shoval O, Kirschner MW, Alon U (2009) The incoherent feedforward loop can provide fold-change detection in gene regulation. *Mol Cell* 36:894–899.
5. Shoval O, et al. (2010) Fold-change detection and scalar symmetry of sensory input fields. *Proc Natl Acad Sci USA* 107:15995–16000.
6. Lazova MD, Ahmed T, Bellomo D, Stocker R, Shimizu TS (2011) Response rescaling in bacterial chemotaxis. *Proc Natl Acad Sci USA* 108:13870–13875.
7. Adler M, Mayo A, Alon U (2014) Logarithmic and power law input-output relations in sensory systems with fold-change detection. *PLoS Comput Biol* 10:e1003781.
8. Kamino K, Kondo Y (2016) Rescaling of spatio-temporal sensing in eukaryotic chemotaxis. *PLoS One* 11:e0164674.
9. Goentoro L, Kirschner MW (2009) Evidence that fold-change, and not absolute level, of beta-catenin dictates Wnt signaling. *Mol Cell* 36:872–884.
10. Wartlick O, et al. (2011) Dynamics of Dpp signaling and proliferation control. *Science* 331:1154–1159.
11. Lee REC, Walker SR, Savery K, Frank DA, Gaudet S (2014) Fold change of nuclear NF-κB determines TNF-induced transcription in single cells. *Mol Cell* 53:867–879.
12. Youk H, Lim WA (2014) Secreting and sensing the same molecule allows cells to achieve versatile social behaviors. *Science* 343:1242782.
13. Dinauer MC, MacKay SA, Devreotes PN (1980) Cyclic 3′,5′-AMP relay in *Dictyostelium discoideum*. III. The relationship of cAMP synthesis and secretion during the cAMP signaling response. *J Cell Biol* 86:537–544.
14. Dinauer MC, Steck TL, Devreotes PN (1980) Cyclic 3′,5′-AMP relay in *Dictyostelium discoideum*. V. Adaptation of the cAMP signaling response during cAMP stimulation. *J Cell Biol* 86:554–561.
15. Dinauer MC, Steck TL, Devreotes PN (1980) Cyclic 3′,5′-AMP relay in *Dictyostelium discoideum*. IV. Recovery of the cAMP signaling response after adaptation to cAMP. *J Cell Biol* 86:545–553.
16. Fukujin F, Nakajima A, Shimada N, Sawai S (2016) Self-organization of chemoattractant waves in *Dictyostelium* depends on F-actin and cell-substrate adhesion. *J R Soc Interface* 13:20160233.
17. Skoge M, et al. (2014) Cellular memory in eukaryotic chemotaxis. *Proc Natl Acad Sci USA* 111:14448–14453.
18. Nakajima A, Ishihara S, Imoto D, Sawai S (2014) Rectified directional sensing in long-range cell migration. *Nat Commun* 5:5367.
19. Alcantara F, Monk M (1974) Signal propagation during aggregation in the slime mould *Dictyostelium discoideum*. *J Gen Microbiol* 85:321–334.
20. Lee KJ, Cox EC, Goldstein RE (1996) Competing patterns of signaling activity in *Dictyostelium discoideum*. *Phys Rev Lett* 76:1174–1177.
21. Hashimoto Y, Cohen MH, Robertson A (1975) Cell density dependence of the aggregation characteristics of the cellular slime mould *Dictyostelium discoideum*. *J Cell Sci* 19:215–229.
22. Gingle AR (1976) Critical density for relaying in *Dictyostelium discoideum* and its relation to phosphodiesterase secretion into the extracellular medium. *J Cell Sci* 20:1–20.
23. Wang B, Kuspa A (1997) *Dictyostelium* development in the absence of cAMP. *Science* 277:251–254.
24. Gregor T, Fujimoto K, Masaki N, Sawai S (2010) The onset of collective behavior in social amoebae. *Science* 328:1021–1025.
25. Kamino K, Fujimoto K, Sawai S (2011) Collective oscillations in developing cells: Insights from simple systems. *Dev Growth Differ* 53:503–517.
26. Sgro AE, et al. (2015) From intracellular signaling to population oscillations: Bridging size- and time-scales in collective behavior. *Mol Syst Biol* 11:779.
27. Börner S, et al. (2011) FRET measurements of intracellular cAMP concentrations and cAMP analog permeability in intact cells. *Nat Protoc* 6:427–438.
28. Masaki N, Fujimoto K, Honda-Kitahara M, Hada E, Sawai S (2013) Robustness of self-organizing chemoattractant field arising from precise pulse induction of its breakdown enzyme: A single-cell level analysis of PDE expression in *Dictyostelium*. *Biophys J* 104:1191–1202.
29. Tomchik KJ, Devreotes PN (1981) Adenosine 3′,5′-monophosphate waves in *Dictyostelium discoideum*: A demonstration by isotope dilution–fluorography. *Science* 212:443–446.
30. Devreotes PN, Potel MJ, MacKay SA (1983) Quantitative analysis of cyclic AMP waves mediating aggregation in *Dictyostelium discoideum*. *Dev Biol* 96:405–415.
31. Garcia GL, Parent CA (2008) Signal relay during chemotaxis. *J Microsc* 231:529–534.
32. Kriebel PW, Barr VA, Rericha EC, Zhang G, Parent CA (2008) Collective cell migration requires vesicular trafficking for chemoattractant delivery at the trailing edge. *J Cell Biol* 183:949–961.
33. Nakajima A, Ishida M, Fujimori T, Wakamoto Y, Sawai S (2016) The microfluidic lighthouse: An omnidirectional gradient generator. *Lab Chip* 16:4382–4394.
34. Postma M, Van Haastert PJM (2016) Mathematics of experimentally generated chemoattractant gradients. *Methods Mol Biol* 1407:381–396.
35. McMains VC, Liao X-H, Kimmel AR (2008) Oscillatory signaling and network responses during the development of *Dictyostelium discoideum*. *Ageing Res Rev* 7:234–248.
36. Sasaki AT, Chun C, Takeda K, Firtel RA (2004) Localized Ras signaling at the leading edge regulates PI3K, cell polarity, and directional cell movement. *J Cell Biol* 167:505–518.
37. Comer FI, Lippincott CK, Masbad JJ, Parent CA (2005) The PI3K-mediated activation of CRAC independently regulates adenylyl cyclase activation and chemotaxis. *Curr Biol* 15:134–139.
38. Comer FI, Parent CA (2006) Phosphoinositide 3-kinase activity controls the chemoattractant-mediated activation and adaptation of adenylyl cyclase. *Mol Biol Cell* 17:357–366.
39. Zhang S, Charest PG, Firtel RA (2008) Spatiotemporal regulation of Ras activity provides directional sensing. *Curr Biol* 18:1587–1593.
40. Iijima M, Devreotes P (2002) Tumor suppressor PTEN mediates sensing of chemoattractant gradients. *Cell* 109:599–610.
41. Brzostowski JA, et al. (2013) Phosphorylation of chemoattractant receptors regulates chemotaxis, actin reorganization and signal relay. *J Cell Sci* 126:4614–4626.
42. Takeda K, et al. (2012) Incoherent feedforward control governs adaptation of activated ras in a eukaryotic chemotaxis pathway. *Sci Signal* 5:ra2.
43. Taniguchi D, et al. (2013) Phase geometries of two-dimensional excitable waves govern self-organized morphodynamics of amoeboid cells. *Proc Natl Acad Sci USA* 110:5016–5021.
44. Fujimoto K, Sawai S (2013) A design principle of group-level decision making in cell populations. *PLoS Comput Biol* 9:e1003110.
45. Skataric M, Sontag ED (2012) A characterization of scale invariant responses in enzymatic networks. *PLoS Comput Biol* 8:e1002748.
46. Adler M, Szekely P, Mayo A, Alon U (2017) Optimal regulatory circuit topologies for fold-change detection. *Cell Syst* 4:171–181.e8.
47. Hamadeh A, Ingalls B, Sontag E (2013) Transient dynamic phenotypes as criteria for model discrimination: Fold-change detection in *Rhodobacter sphaeroides* chemotaxis. *J R Soc Interface* 10:20120935.
48. Iglesias PA, Shi C (2014) Comparison of adaptation motifs: Temporal, stochastic and spatial responses. *IET Syst Biol* 8:268–281.
49. Shankar P, Nishikawa M, Shibata T (2015) Adaptive responses limited by intrinsic noise. *PLoS One* 10:e0136095.
50. Martiel JL, Goldbeter A (1987) A model based on receptor desensitization for cyclic AMP signaling in *Dictyostelium* cells. *Biophys J* 52:807–828.
51. Tang Y, Othmer HG (1994) A G protein-based model of adaptation in *Dictyostelium discoideum*. *Math Biosci* 120:25–76.
52. Zhang M, Goswami M, Sawai S, Cox EC, Hereld D (2007) Regulation of G protein-coupled cAMP receptor activation by a hydrophobic residue in transmembrane helix 3. *Mol Microbiol* 65:508–520.
53. Insall RH, Soede RD, Schaap P, Devreotes PN (1994) Two cAMP receptors activate common signaling pathways in *Dictyostelium*. *Mol Biol Cell* 5:703–711.
54. Aldridge J, Pye EK (1976) Cell density dependence of oscillatory metabolism. *Nature* 259:670–671.
55. Richards DM, Saunders TE (2015) Spatiotemporal analysis of different mechanisms for interpreting morphogen gradients. *Biophys J* 108:2061–2073.
56. Ishimatsu K, Takamatsu A, Takeda H (2010) Emergence of traveling waves in the zebrafish segmentation clock. *Development* 137:1595–1599.
57. Tsiairis CD, Aulehla A (2016) Self-organization of embryonic genetic oscillators into spatiotemporal wave patterns. *Cell* 164:656–667.
58. Sawai S, Thomason PA, Cox EC (2005) An autoregulatory circuit for long-range self-organization in *Dictyostelium* cell populations. *Nature* 433:323–326.
59. Nikolaev VO, Bünemann M, Hein L, Hannawacker A, Lohse MJ (2004) Novel single chain cAMP sensors for receptor-induced signal propagation. *J Biol Chem* 279:37215–37218.
60. Gordon GW, Berry G, Liang XH, Levine B, Herman B (1998) Quantitative fluorescence resonance energy transfer measurements using fluorescence microscopy. *Biophys J* 74:2702–2713.
61. Xia Z, Liu Y (2001) Reliable and global measurement of fluorescence resonance energy transfer using fluorescence microscopes. *Biophys J* 81:2395–2402.
62. Nakajima A, Sawai S (2016) Dissecting spatial and temporal sensing in *Dictyostelium* chemotaxis using a wave gradient generator. *Methods Mol Biol* 140:107–122.
63. Postma M, et al. (2003) Uniform cAMP stimulation of *Dictyostelium* cells induces localized patches of signal transduction and pseudopodia. *Mol Biol Cell* 14:5019–5027.
64. Goldbeter A (1996) *Biochemical Oscillations and Cellular Rhythms: The Molecular Bases of Periodic and Chaotic Behaviour* (Cambridge Univ Press, Cambridge, UK).
65. Tyson JJ, Murray JD (1989) Cyclic AMP waves during aggregation of *Dictyostelium* amoebae. *Development* 106:421–426.
66. Tyson JJ, Alexander KA, Manoranjan VS, Murray JD (1989) Spiral waves of cyclic AMP in a model of slime mold aggregation. *Physica D* 34:193–207.

67. Pálsson E, Cox EC (1996) Origin and evolution of circular waves and spirals in *Dictyostelium discoideum* territories. *Proc Natl Acad Sci USA* 93:1151–1155.
68. Lauzeral J, Halloy J, Goldbeter A (1997) Desynchronization of cells on the developmental path triggers the formation of spiral waves of cAMP during *Dictyostelium* aggregation. *Proc Natl Acad Sci USA* 94:9153–9158.
69. Geberth D, Hütt M-T (2009) Predicting the distribution of spiral waves from cell properties in a developmental-path model of *Dictyostelium* pattern formation. *PLoS Comput Biol* 5:e1000422.
70. Pálsson E (2009) A cAMP signaling model explains the benefit of maintaining two forms of phosphodiesterase in *Dictyostelium*. *Biophys J* 97:2388–2398.